Dalton Transactions

ROYAL SOCIETY OF CHEMISTRY

PAPER

View Article Online
View Journal | View Issue

Cite this: *Dalton Trans.*, 2026, **55**, 1169

Engineering Fe_3O_4–Fe_3C/C heterojunction nanosheets with multimodal therapy for tumor microenvironment-programmed drug delivery and enhanced chemodynamic therapy

Desheng Wang,†[a] Changjin Xu, *†[a] Shikui Wu, [a] Gang Li,[a] Huiwen Zhang,[a] Herima Qi,[a] Riqing Cheng,[a] Liang Bao,[b] Huiqing Guo*[a] and Jianping Chen*[a]

Received 24th October 2025,
Accepted 22nd December 2025

DOI: 10.1039/d5dt02555a

rsc.li/dalton

Fe_3O_4–iron carbide composites offer promising cancer therapeutic potential *via* magnetic targeting and tumor-responsive Fe^{2+} release. However, current synthesis methods suffer from complex multi-step procedures, toxic reagents, and poor biocompatibility, necessitating additional surface modifications. Herein, we developed a facile and green strategy to synthesize Fe_3O_4–Fe_3C composites through tannic acid–Fe^{3+} coordination, pyrolysis, and HCl etching. The resulting Fe_3O_4–Fe_3C/C heterojunction composite possesses high saturation magnetization, large specific surface area, and strong Fe–carbon interfacial interactions, which collectively enhance magnetic targeting, drug loading capacity, and Fenton reaction kinetics for amplified chemodynamic therapy. Following polydopamine (PDA) coating and 5-fluorouracil (5-FU) loading, the Fe_3O_4–Fe_3C/C@5-FU@PDA system achieved 55.6% loading efficiency with pH-responsive release (76.1% at pH 5.0 over 48 h). Under 808 nm NIR irradiation (2 W cm^{-2}, 120 s), the system demonstrated efficient photothermal conversion, elevating tumor temperatures to 45.4 °C for thermal ablation. Both *in vitro* and *in vivo* studies confirm superior tumor inhibition *via* synergistic chemotherapy, photothermal therapy (PTT), and chemodynamic therapy (CDT).

1. Introduction

Cancer remains a global health threat, with therapeutic strategies evolving from traditional monomodal approaches toward multimodal synergistic regimens.[1–3] Although surgery, radiotherapy, and chemotherapy (*e.g.*, 5-FU) remain mainstream interventions, their clinical efficacy is compromised by systemic toxicity, poor tumor selectivity, and drug resistance.[4–6] Recent advances in nanomedicine have enabled the development of stimulus-responsive multifunctional delivery systems, offering new paradigms for synergistic enhancement of CDT, PTT, and chemotherapy.[7–11] These systems leverage tumor microenvironment (TME) characteristics (*e.g.*, mild acidity, elevated H_2O_2 levels) to achieve spatiotemporal drug release control while facilitating tumor-specific accumulation through cascade catalytic reactions, energy conversion, and multimodal therapeutic interactions.[12–14]

Magnetite (Fe_3O_4) nanoparticles have been extensively investigated for constructing tumor-targeted nanoplatforms due to their superior magnetic responsiveness, biocompatibility, and catalytic properties.[15,16] Fe_3O_4-based supports enable magnetic field-guided active tumor targeting to enhance therapeutic accumulation.[17,18] Simultaneously, Fe_3O_4 can catalyze the decomposition of H_2O_2 into hydroxyl radicals ($^{\bullet}OH$) *via* Fenton-like reactions, inducing oxidative damage and apoptosis in cancer cells for CDT.[2,19] However, conventional Fe_3O_4 nanomaterials face several limitations: their relatively low saturation magnetization compromises magnetic targeting efficiency, leading to insufficient accumulation at tumor sites, while their restricted photothermal conversion efficiency hinders their application in effective photothermal therapy.[20,21]

Iron carbide nanoparticles (ICNPs), as iron-carbon intermetallic compounds, have demonstrated significant potential in cancer theranostics owing to their unique physicochemical properties.[22] Compared to metallic iron nanoparticles, the incorporation of carbon atoms into the interstitial sites of the iron lattice in ICNPs confers greater stability, potentially improving biosafety and service life.[23] Their high saturation magnetization (~140 emu g^{-1}) further broadens applications in biomedicine and magnetic data

[a]*College of Pharmacy, Inner Mongolia Medical University, Hohhot 010110, China. E-mail: changjin.xu@immu.edu.cn, ghq5@163.com, jianping5817@163.com*
[b]*Medical Innovation Center for Nationalities, Inner Mongolia Medical University, Hohhot 010110, China*
† These authors contributed equally and should be considered co-first authors.

storage.[22] For instance, Hou *et al.*[24] developed core–shell structured Fe_5C_2 nanoparticles for cancer theranostics, where the carbon shell effectively preserved high magnetic properties, enabling excellent magnetic resonance imaging performance. Yu *et al.*[22] synthesized Fe_5C_2@Fe_3O_4 magnetic nanozymes that functioned as reactive oxygen species reactors, achieving efficient magnetic targeting and tumor microenvironment-activated Fe^{2+} release for enhanced cancer therapy. Despite these advantages, current synthesis methods for Fe_5C_2@Fe_3O_4 nanocomposites typically involve multi-step high-temperature reactions, toxic precursors and organic solvents. Thus, developing a facile and green synthesis strategy for Fe_3O_4–iron carbide composites remains highly desirable.

Herein, we developed a facile strategy to synthesize Fe_3O_4–Fe_3C/C heterojunction nanosheets (FFC2) *via* tannic acid/Fe^{3+} coordination, calcination, and etching, as illustrated in Scheme 1. The FFC2 material integrates a carbon layer for enhanced drug loading, and a pH-responsive architecture for synergistic drug/Fe^{2+} release. The strong Fe_3C–carbon interaction promotes electron transfer, accelerating Fe^{2+} regeneration and Fenton reaction kinetics for amplified CDT. After loading 5-FU and coating with PDA, the resulting FFC2@FU@PDA material achieved a 55.6% drug loading efficiency and 63.5% photothermal conversion efficiency. This FFC2@FU@PDA composite demonstrates remarkable antitumor efficacy both *in vitro* and *in vivo*, inducing ~15-fold higher apoptosis and significant tumor suppression, thereby establishing a promising multimodal therapy platform.

2. Experimental details

2.1. Materials

All chemicals and reagents used in this study were of analytical grade and used as received without further purification. The detailed information of materials and reagents is provided in the SI.

2.2. Synthesis of FFC*x* nanocomposites

The FFC*x* nanomaterials were synthesized through the following procedure: TA and $FeCl_3$ were separately dissolved in ultrapure water at a concentration ratio of 1 : 20. The $FeCl_3$ solution was gradually poured into the TA solution under continuous stirring, followed by dropwise addition of $NaHCO_3$ solution to adjust the pH to 7. The mixture was allowed to stand until black precipitates were completely formed. The precipitates were collected by centrifugation, washed three times with ultrapure water, and freeze-dried to obtain TA-Fe powders. Subsequently, these powders were then reduced under H_2 atmosphere through calcination at 400, 600, 800, or 900 °C for 2 h (heating rate: 5 °C min^{-1}), yielding composites composed of Fe_3O_4 at 400 and 600 °C (labeled as Fe_3O_4-400 and Fe_3O_4-600) or Fe–Fe_3C/C at 800 and 900 °C (labeled as Fe–Fe_3C/C-800 and Fe–Fe_3C/C-900). Next, the Fe–Fe_3C/C-800 obtained above was etched in HCl solutions with different volume percentages (1%, 2%, 3%) for 2 h. Finally, the products were washed three times with distilled water and anhydrous ethanol, respectively, resulting in the Fe_3O_4–Fe_3C/C composite materials, which were named FFC*x* nanomaterials (where *x* denotes the volume percentage of HCl employed).

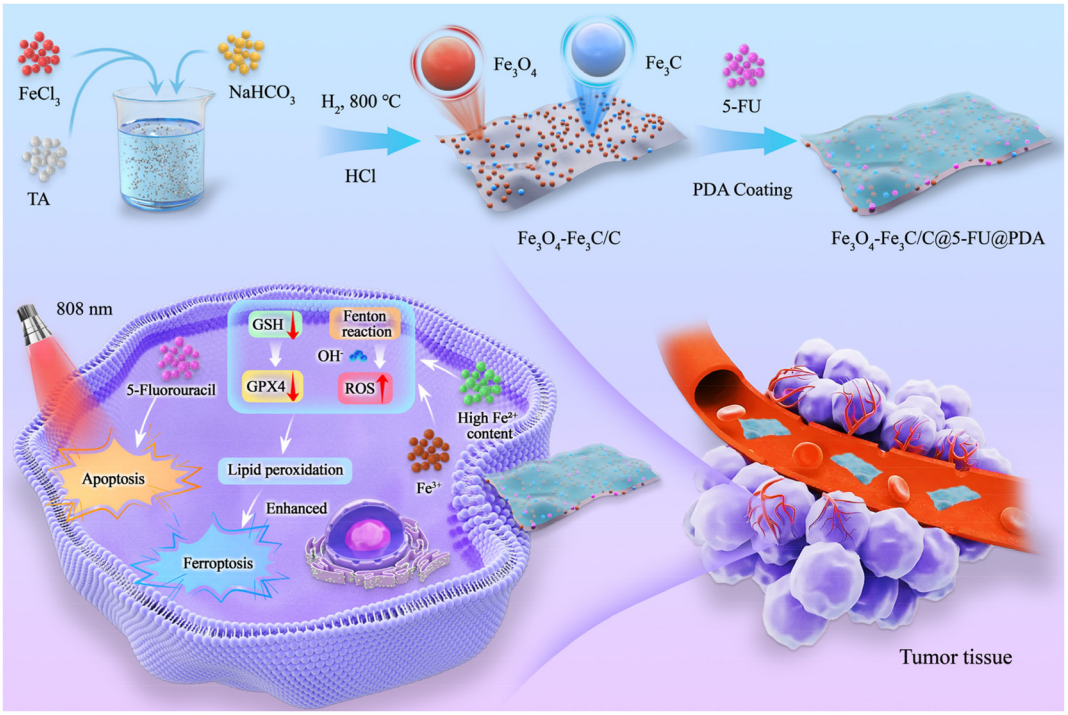

Scheme 1 Schematic illustration of FFC2@FU@PDA nanomaterial synthesis and the combined chemotherapy-PTT-CDT for tumor inhibition.

2.3. Synthesis of FFC2@FU materials

The loading of 5-FU chemotherapeutic drug onto FFC2 nanocomposite materials was carried out as follows. Initially, FFC2 was uniformly dispersed in a methanol–water mixed solvent to form a stable suspension. Subsequently, 5-FU was added to the suspension, with the mass ratios of FFC2 to 5-FU systematically adjusted to 2 : 1, 1 : 1, 1 : 2, 1 : 3, 1 : 4, and 1 : 5, respectively. The mixtures were continuously stirred at room temperature for different durations (1, 4, 6, 8, 12, 14 and 16 h). After the reaction was completed, the supernatant and precipitate were collected by centrifugation. The resulting precipitate was thoroughly washed three times with distilled water to effectively remove unabsorbed 5-FU. Finally, the 5-FU-loaded FFC2 nanocomposite material was obtained, denoted as FFC2@5-FU (abbreviated as FFC2@FU).

2.4. Synthesis of FFC2@FU@PDA materials

An appropriate amount of FFC2@FU powder was dissolved in ultrapure water to prepare a 1 mg mL^{-1} FFC2@FU solution, while dopamine hydrochloride powder was dissolved in Tris-HCl buffer (pH 8.5) and prepared as a 2 mg mL^{-1} solution. The two solutions were then mixed at an equal volume ratio, stirred at room temperature for 24 h, centrifuged, washed, and the resulting precipitate was vacuum-dried at 40 °C for 24 h, yielding the final product designated as FFC2@FU@PDA.

2.5. Materials characterization and *in vitro* evaluation

The comprehensive characterization of the materials (including structural, morphological, surface, and magnetic properties) and systematic *in vitro* evaluations (such as drug loading/release behavior, Fe^{2+} release, $^{\bullet}OH$ generation, photothermal properties, cellular uptake, cytotoxicity, migration inhibition, ROS detection, apoptosis analysis, and hemocompatibility) have been completed. Detailed experimental methods and conditions refer to the SI.

3. Results and discussion

3.1. Preparation and characterization of the as-prepared materials

To investigate the crystal structure of the prepared materials, XRD analysis was performed on TA-Fe powders calcined under different temperatures in hydrogen atmospheres (Fig. S1). The results showed that at low calcination temperatures of 400 °C and 600 °C, the main product is Fe_3O_4 oxide. However, when the temperature was increased to 800 °C or 900 °C, the product transformed into a mixture of metallic Fe, Fe_3C, and carbon. Due to the high biotoxicity risk of metallic Fe, the Fe–Fe_3C/C-800 material calcined at 800 °C was subjected to HCl etching to selectively remove metallic Fe.[20] As shown in Fig. 1a, treatment with 2% or 3% dilute HCl completely remove metallic Fe, resulting in the formation of Fe_3O_4–Fe_3C/C composite materials. Based on the content of Fe_3C in the Fe_3O_4–Fe_3C/C material, the FFC2 material etched with 2% HCl was selected for subsequent drug-loading and surface modification studies. Furthermore, the diffraction peak positions of FFC2@FU@PDA sample remain unchanged, with only slight reduction in peak intensity, which can be attributed to the masking effect of the PDA coating layer. These results confirm the successful encapsulation of PDA on the FFC2@FU composite surface (Fig. 1a). The FTIR spectrum reveals a characteristic peak at 1280 cm^{-1}, attributed to aromatic ring vibrations of PDA, which persists in the FFC2@FU@PDA composite, confirming successful PDA coating (Fig. S2). While pure 5-FU exhibits a distinct C–F stretching peak at 1242 cm^{-1},[25] the absence of this characteristic signal in the composite suggests highly dispersed 5-FU molecules on the FFC2 support surface.

SEM morphological analysis reveals coexisting bulk particles and nanosheets in pristine Fe–Fe_3C/C-800 (Fig. 1b), while the etched FFC2 exclusively maintains nanosheet morphology with eliminated large particles (Fig. 1c). TEM and HAADF-STEM characterization further unveils uniformly distributed ~20 nm nanoparticles on FFC2 nanosheets (Fig. 1d and e). Combined with elemental mapping analysis (Fig. 1f), the nanosheet substrate is identified as carbon, while surface nanoparticles comprise dual-phase Fe_3O_4 and Fe_3C, consistent with XRD results. This hierarchical nanosheet-nanoparticle architecture could significantly enhance specific surface area, thereby increasing the drug-loading capacity.[26] Furthermore, TEM analysis reveals that FFF2@FU@PDA maintains the original nanosheet morphology of FFC2 after 5-FU loading and PDA coating. Elemental mapping demonstrates uniform distribution of F element across the material surface, confirming homogeneous drug dispersion throughout the support. And the significantly higher N element content compared to F element content can be attributed to the additional nitrogen contribution from the PDA structure, providing strong evidence of successful PDA encapsulation on the material surface (Fig. S3). Dynamic Light Scattering (DLS) analysis shows the respective size distribution of FFC2 and the functionalized FFC2@FU@PDA to be 600–800 nm and 500–1000 nm (Fig. S4a and b). Meanwhile, the FFC2 and FFC2@FU@PDA exhibit high colloidal stability, showing negligible size variation over a 7 day incubation in PBS (Fig. S4c).

To quantitatively characterize the specific surface area of the material, nitrogen adsorption–desorption tests were conducted on a series of samples. The nitrogen adsorption–desorption isotherms of Fe–Fe_3C/C-800, FFC2, and FFC2@FU@PDA, exhibit Type IV isotherms with H3 hysteresis loops in the relative pressure range of 0.4–1.0 (Fig. 1g), consistent with the IUPAC definition of slit-shaped mesoporous structures.[27] Specific surface area analysis shows that Fe–Fe_3C/C-800 has a specific surface area of 146.2 $m^2\ g^{-1}$, which increases to 168.38 $m^2\ g^{-1}$ after etching in FFC2 due to the exposure of the nanosheet structure. After loading FU and coating with PDA, the specific surface area of FFC2@FU@PDA significantly increases to 686.88 $m^2\ g^{-1}$, primarily attributed to the additional mesopores introduced by the PDA layer. The abundant mesoporous structure not only provides a high specific surface area but also creates channels for drug molecule diffusion, suggesting potential applications in drug delivery.[28]

XPS analysis of Fe 2p spectra (Fig. 1h) verifies chemical states critical for chemodynamic therapy. As shown in Fig. S5a,

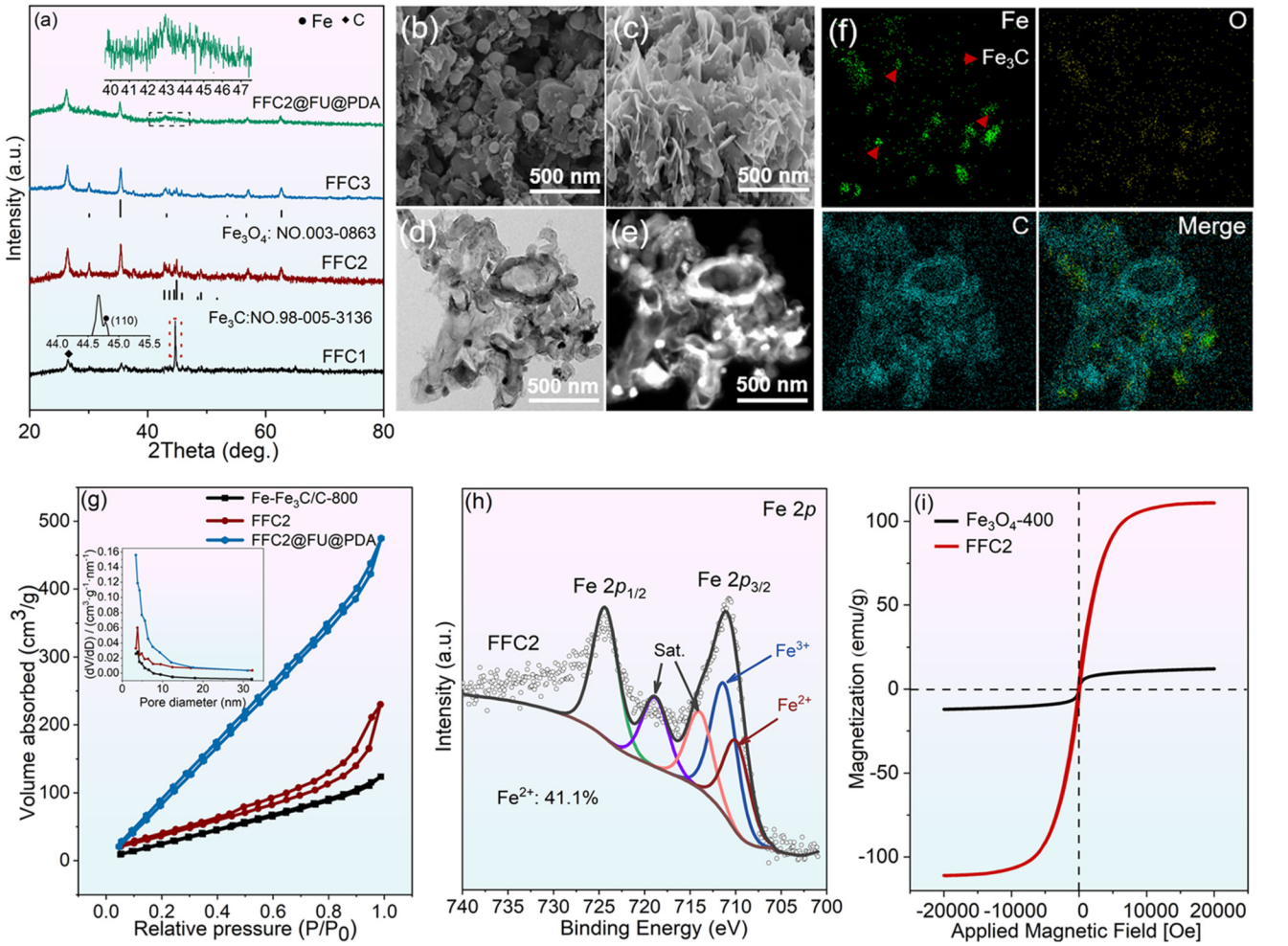

Fig. 1 Structural characterization of the materials. (a) XRD patterns of FFC1, FFC2, FFC3 and FFC2@FU@PDA. SEM images of the Fe–Fe_3C/C-800 (b) and FFC2 (c) materials. (d) TEM image of FFC2 material. (e) HAADF-STEM image of FFC2 material. (f) Elemental mapping of FFC2 based on HAADF-STEM. (g) Nitrogen adsorption–desorption isotherms of FFC2 (inset: pore size distribution); (h) Fe 2p XPS spectrum of the FFC2 materials. (i) Hysteresis loop curves of Fe_3O_4-400 and FFC2 materials.

the deconvoluted O 1s spectrum exhibits two resolved components: the lower binding energy peak at 530.0 eV corresponds to lattice oxygen in Fe–O bonds, while the higher energy peak at 531.1 eV arises from Fe–O–C interfacial coordination.[29] The dominant Fe–O–C bonding confirms strong chemical coupling between Fe species and the carbon matrix, effectively suppressing nanoparticle aggregation through structural stabilization. This interfacial synergy not only enhances material durability but also facilitates directional electron transfer from the carbon substrate to Fe active sites, thereby accelerating the reduction of Fe^{3+} to Fe^{2+} and optimizing redox activity for catalytic processes,[30] as illustrated in Fig. S5b. Furthermore, deconvolution of characteristic peaks at 711.1 eV (Fe $2p_{3/2}$) and 724.4 eV (Fe $2p_{1/2}$) identifies Fe^{2+} (709.7 eV) and Fe^{3+} (711.4 eV) species.[31] Quantitative analysis indicated that there is a high concentration of Fe^{2+} species on the surface of FFC2, approximately 41.1%, which may be due to the enhanced interaction between iron species and the carbon support, which promotes electron transfer from the carbon to the iron species.[30] Therefore, unlike conventional Fe-based nanozymes,[32,33] this Fe_3O_4–Fe_3C/C heterojunction anchors dual-phase nanoparticles onto carbon nanosheets, fostering strong Fe–O–C interfacial interactions. This design not only augments drug capacity and active sites *via* a large surface area but also achieves superior chemodynamic performance through structural synergy. Due to the weakly acidic nature and high H_2O_2 expression in the tumor microenvironment,[12,13] the high Fe^{2+} content can promote the catalytic reaction between Fe^{2+} and H_2O_2 in the tumor microenvironment, generating more $^{\bullet}OH$ radicals and thereby enhancing tumor cell apoptosis efficiency.[34,35]

VSM measurements (Fig. 1i) demonstrate ferromagnetic behavior for both Fe_3O_4-400 and FFC2, with the latter exhibiting superior saturation magnetization. This enhancement is attributed to the intrinsic ferromagnetic nature of the Fe_3C phase present in FFC2, which enables parallel alignment of all magnetic moments without significant cancellation. In contrast, the ferrimagnetic Fe_3O_4 possesses an inverse spinel structure where opposing magnetic moments on tetrahedral and octa-

hedral sublattices lead to partial cancellation, resulting in a lower net saturation magnetization.

Therefore, the high saturation magnetization of this material not only facilitates magnetic targeting delivery but also indicates its potential as a T_2-weighted MRI contrast agent, offering possibilities for theranostic applications. In summary, FFC2 nanosheet was developed through calcination and HCl etching of TA-Fe precursors. The resultant material integrates high surface area, Fe^{2+}-enriched composition, and strong magnetism, enabling simultaneous realization of high drug loading capacity, efficient $^{\bullet}OH$ generation, and magnetically targeted delivery. This multifunctional platform presents novel opportunities for advanced tumor therapy.

3.2. *In vitro* catalytic activity and drug loading/release behavior

The Fenton reaction, mediated by Fe^{2+}, catalyzes the conversion of intracellularly generated H_2O_2 into highly toxic $^{\bullet}OH$, thereby inducing cellular apoptosis. Its activity exhibits positive correlation with Fe^{2+} concentration in the tumor microenvironment. Given the slow reduction kinetics of Fe^{3+} by H_2O_2, maintaining elevated Fe^{2+} levels is critical for enhancing Fenton reaction efficiency.[36] To validate the performance of FFC2, Fe^{2+} release efficiency was first examined in PBS media with varying pH values (mimicking physiological conditions). As shown in Fig. 2a, FFC2 demonstrates significantly higher Fe^{2+} release under acidic conditions (pH 5.0, simulating tumor microenvironment) compared to neutral (pH 7.4, normal tissue) and mildly acidic (pH 6.3) environments, confirming its pH-responsive Fe^{2+} release specificity. To investigate the Fe^{2+} release kinetics, we conducted time-dependent release experiments at pH 5.0. As shown in Fig. S6, the concentration of released Fe^{2+} gradually increases with time and reaches a plateau after 12 h, with no significant difference observed between the 12 h and 18 h time points. This indicates that the Fe^{2+} release achieved saturation at approximately 12 h under these conditions. Furthermore, as shown in Fig. 2b, even after drug loading and PDA coating treatment, the FFC2@FU@PDA

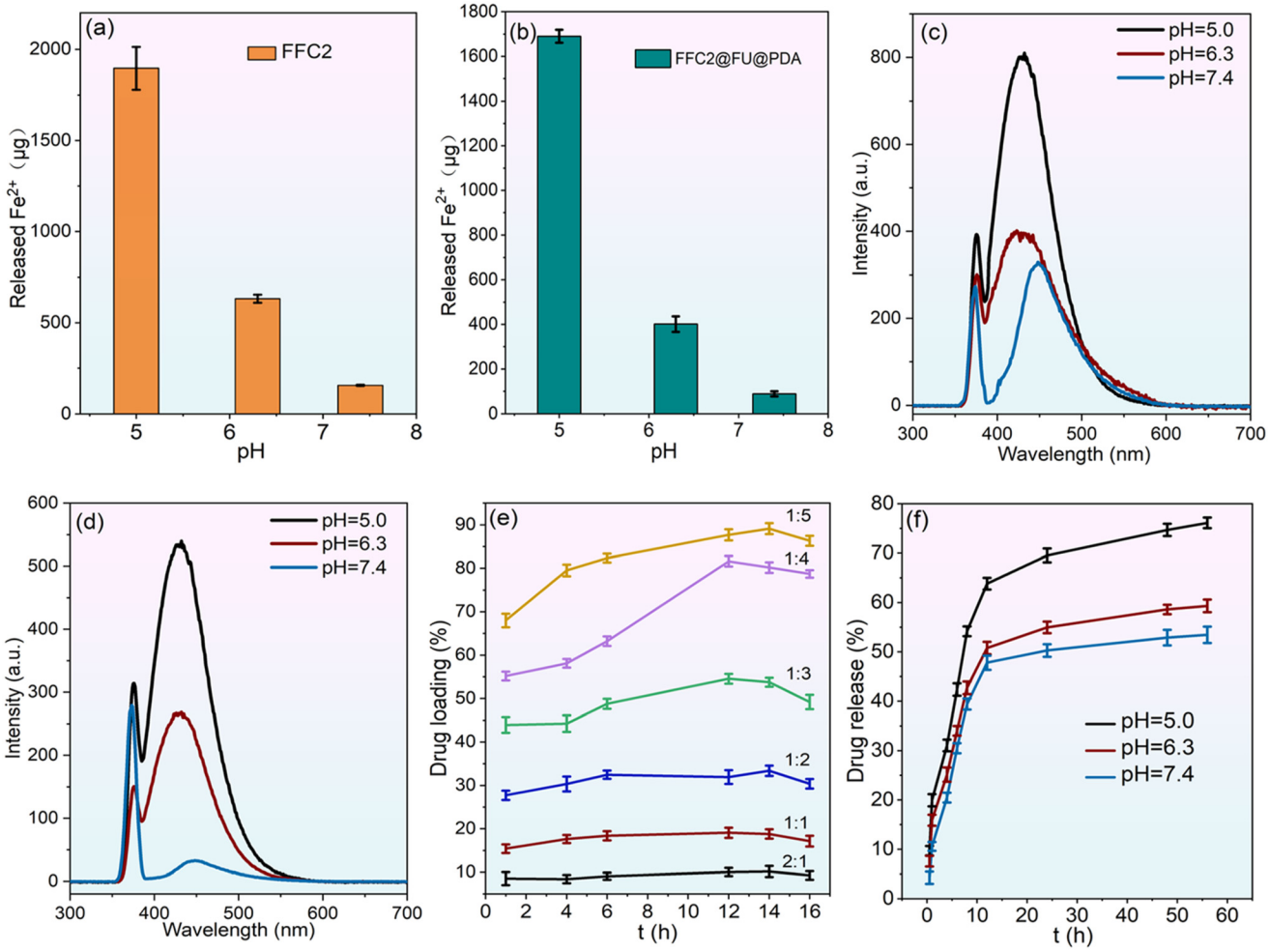

Fig. 2 Fe^{2+} release from FFC2 (a) and FFC2@FU@PDA (b) at 12 h under different pH values. $^{\bullet}OH$ generation by FFC2 (c) and FFC2@FU@PDA (d) at different pH values. (e) Drug-loading capacity of FFC2 over time at different material-to-drug ratios. (f) 5-FU release rate of FFC2@FU@PDA at different pH values.

system still maintains a high release amount of Fe^{2+} under pH 5.0 acidic conditions. This result indicates that neither the drug loading process nor the formation of the PDA coating layer significantly impedes the release capability of Fe^{2+} in an acidic environment. Building on this property, $^{\bullet}OH$ generation was quantified using hydroxyl radical probes across pH conditions (5.0, 6.3, 7.4). As shown in Fig. 2c and d, both FFC2 and FFC2@FU@PDA exhibit high $^{\bullet}OH$ concentrations under pH 5.0 conditions, with trends mirroring their Fe^{2+} release profiles. These results confirm that acidic microenvironment-triggered Fe^{2+} release from FFC2 amplifies Fenton reaction efficacy, promoting tumor cell apoptosis through $^{\bullet}OH$ accumulation. Furthermore, as shown in Fig. S7, given the presence of Fe^{3+} oxidation states in the redox process, the glutathione (GSH) depletion activity of FFC2 and FFC2@FU@PDA exhibits significant pH dependency. In the tumor microenvironment (pH = 5.0), both FFC2 and FFC2@FU@PDA demonstrate excellent GSH depletion capabilities. Collectively, the synergistic interplay between tumor microenvironment-specific responsiveness and Fe^{2+}-enhanced catalytic H_2O_2 conversion establishes FFC2's superior chemodynamic therapeutic potential.

Leveraging FFC2's high surface area, 5-FU was employed as a model drug to evaluate loading performance. Since drug molecules typically adsorb *via* non-covalent interactions, including van der Waals forces and hydrogen bonding, zeta potential analysis was conducted to monitor surface charge evolution. As illustrated in Fig. S8, stepwise material modification induces progressive zeta potential shifts: FFC2@FU exhibits marked potential elevation *versus* pristine FFC2, confirming successful drug adsorption, while subsequent PDA coating reduces potential significantly due to PDA's low isoelectric point, verifying complete encapsulation. Notably, higher absolute zeta potential values enhance interparticle electrostatic repulsion, improving colloidal dispersion stability.[37] Consequently, FFC2@FU@PDA demonstrates exceptional stability in solution.

To optimize the drug loading performance of FFC2, loading capacity under different material-to-drug ratios was systematically investigated (Fig. 2e). As shown in Fig. 2e, the drug loading rate gradually increased with increasing material-to-drug ratio. Determined according to the 5-FU standard curve (Fig. S9a). At a ratio of 1 : 5, the drug loading capacity of FFC2 reaches 90% after 14 h, while at a ratio of 1 : 4, a loading capacity of 80% was achieved within 12 h. Based on economic considerations (reducing raw material consumption and shortening preparation time), a ratio of 1 : 4 with a loading time of 12 h was selected as the optimal condition for preparing FFC2@FU for subsequent PDA coating. It should be noted that the PDA coating process could led to some drug loss. Quantitative analysis revealed that the final drug loading rate of FFC2@FU@PDA was 55.6%±1.03%, which remains significantly higher than values reported in similar studies.[2,7,38,39] This high loading capacity arises primarily from the ultrahigh specific surface area of the material, complemented by synergistic non-covalent interactions. To assess tumor microenvironment-responsive drug release, 5-FU release profiles from FFC2@FU@PDA were evaluated in PBS solutions (pH 5.0–7.4). As depicted in Fig. 2f, the composite exhibits pH-dependent release characteristics, achieving maximum cumulative release (76.12 ± 1.18%) at pH 5.0 over 48 h. The enhanced acidic release stems from protonation of 5-FU and pH-triggered PDA layer decomposition, which accelerates desorption kinetics.[33] This selective responsiveness to tumor microenvironment acidity provides critical assurance for precision drug delivery.

3.3. Photothermal performance

The photothermal conversion properties of FFC2@FU@PDA with high magnetic saturation intensity were investigated using an 808 nm near-infrared laser (Fig. 3). The temperature–time curves reveal distinct concentration-dependent and power density-dependent heating effects for FFC2@FU@PDA (Fig. 3a and b). Under optimized conditions (200 μg mL^{-1}, 2.0 W cm^{-2}), comparative analysis demonstrated negligible differences in photothermal performance between FFC2@FU and FFC2 at identical particle concentrations and irradiation durations. However, the PDA-coated FFC2@FU@PDA exhibits significantly superior performance compared to FFC2@FU, which can be attributed to the intrinsic photothermal conversion capability of the PDA coating layer itself (Fig. 3c). Previous studies have confirmed that tumor cells experience hyperthermia-mediated therapeutic effects at temperatures >42 °C, while irreversible thermal ablation requires temperatures exceeding 56 °C.[13,40] Experimental results demonstrate that under NIR irradiation, FFC2@FU@PDA nanoparticles rapidly elevate temperature from 20 °C to 45.4 °C within 2 min, reaching the hyperthermia range (>42 °C) that induces tumor cell sensitization. Crucially, the temperature attains ~56 °C at ~3 min, exceeding the critical threshold for irreversible thermal ablation where instantaneous protein denaturation and coagulative necrosis occur. This rapid photothermal response ensures efficient tumor eradication. Furthermore, the photothermal heating effect elevates local temperature at tumor sites, which promotes blood circulation, alleviates hypoxia, and mitigates drug resistance caused by hypoxic microenvironments, thereby enhancing the synergistic therapeutic efficacy of nanodrug carriers.[40]

To further evaluate the photothermal conversion efficiency, the heating and cooling trends of FFC2@FU@PDA, FFC2@FU and FFC2 particles were recorded after 5 min of NIR irradiation followed by natural cooling (Fig. 3d). Based on the established formula,[41,42] the photothermal conversion efficiency of different materials was systematically investigated. FFC2 and FFC2@FU show photothermal conversion efficiencies of 60.6% and 60.1%, respectively. After PDA coating, FFC2@FU@PDA exhibits the highest photothermal conversion efficiency of 66.7%, outperforming most reported nanomaterials in this category.[2,13,19,25,41] This enhancement is attributed to the synergistic photothermal contributions from both the Fe_3O_4–Fe_3C heterojunction nanoparticles and the PDA shell, as well as the improved light absorption and thermal conductivity afforded by the carbon nanosheet architecture. Fitting of the cooling curve for the 200 μg mL^{-1}

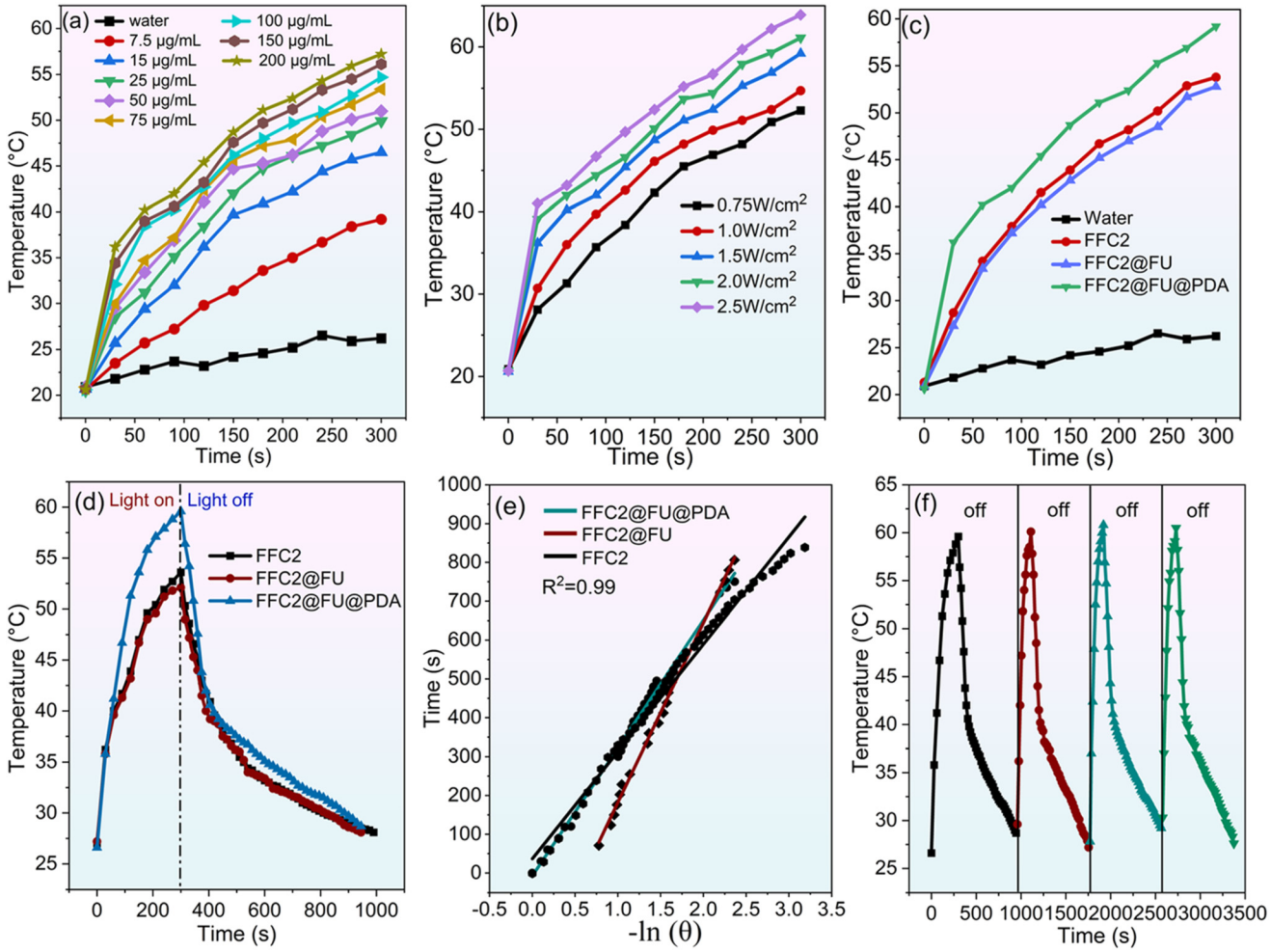

Fig. 3 (a) Temperature *vs.* time curves of FFC2@FU@PDA at different concentrations under a power density of 2.0 W cm^{-2}. (b) Temperature *vs.* time curves of FFC2@FU@PDA at various power densities with a solution concentration of 200 μg mL^{-1}. (c) Temperature *vs.* time curves of different materials under a power density of 2.0 W cm^{-2} and a concentration of 200 μg mL^{-1}. (d) Heating and cooling curves of FFC2@FU@PDA, FFC2 and FFC2@FU particle suspension (200 μg mL^{-1}, 2.0 W cm^{-2}). (e) Plot of cooling time *versus* temperature driving force for FFC2@FU@PDA, FFC2 and FFC2@FU particles. (f) Four heating–cooling cycles of FFC2@FU@PDA (200 μg mL^{-1}, 2.0 W cm^{-2}).

FFC2@FU@PDA, FFC2 and FFC2@FU nanoparticle suspension yields a time constant (τ_s) of 329.4, 276.3 and 264.3 (Fig. 3e), respectively. The photothermal stability of FFC2@FU@PDA was assessed over four laser on/off cycles, with no significant temperature variation observed (Fig. 3f), confirming its excellent operational stability. In summary, FFC2@FU@PDA exhibits highly efficient and stable photothermal conversion characteristics. Its rapid heating capability and tunable temperature response provide an ideal platform for precision photothermal therapy.

3.4. *In vitro* cytotoxicity assessment

Due to the inherent lack of fluorescence in FFC2 and FFC2@FU@PDA nanomaterials, RhoB was loaded to investigate their cellular uptake behavior. As shown in Fig. 4a, the enhanced red fluorescence intensity of drug-loaded FFC2@FU@PDA in cells compared to non-loaded FFC2 demonstrates that 5-FU facilitates cellular uptake, primarily due to the nanodrug delivery system penetrating the cell membrane *via* non-specific endocytosis, whereas its drug-free counterpart relies on passive diffusion.[43] Quantitative analysis (Fig. 4b) further confirms that the FFC2@FU@PDA group exhibited higher fluorescence intensity than the FFC2 group, demonstrating that 5-FU drug-loaded markedly improves cellular internalization efficiency. Notably, NIR laser irradiation further amplified the fluorescence signal, which may be attributed to transient laser-induced membrane permeabilization, thereby facilitating transmembrane transport of nanoparticles.[44]

Excellent biocompatibility is a prerequisite for the application of nanomaterials in *in vivo* therapy. Cytotoxicity evaluation of FFC2 reveals that cell viability remained above 80% even at the highest concentration (200 μg mL^{-1}) after 24 h of incubation (Fig. 4c), confirming the excellent biosafety of FFC2 and its suitability as a nanodrug delivery platform. In stark contrast, the chemotherapeutic drug 5-FU exhibits concentration-dependent cytotoxic effects, with cell viability decreas-

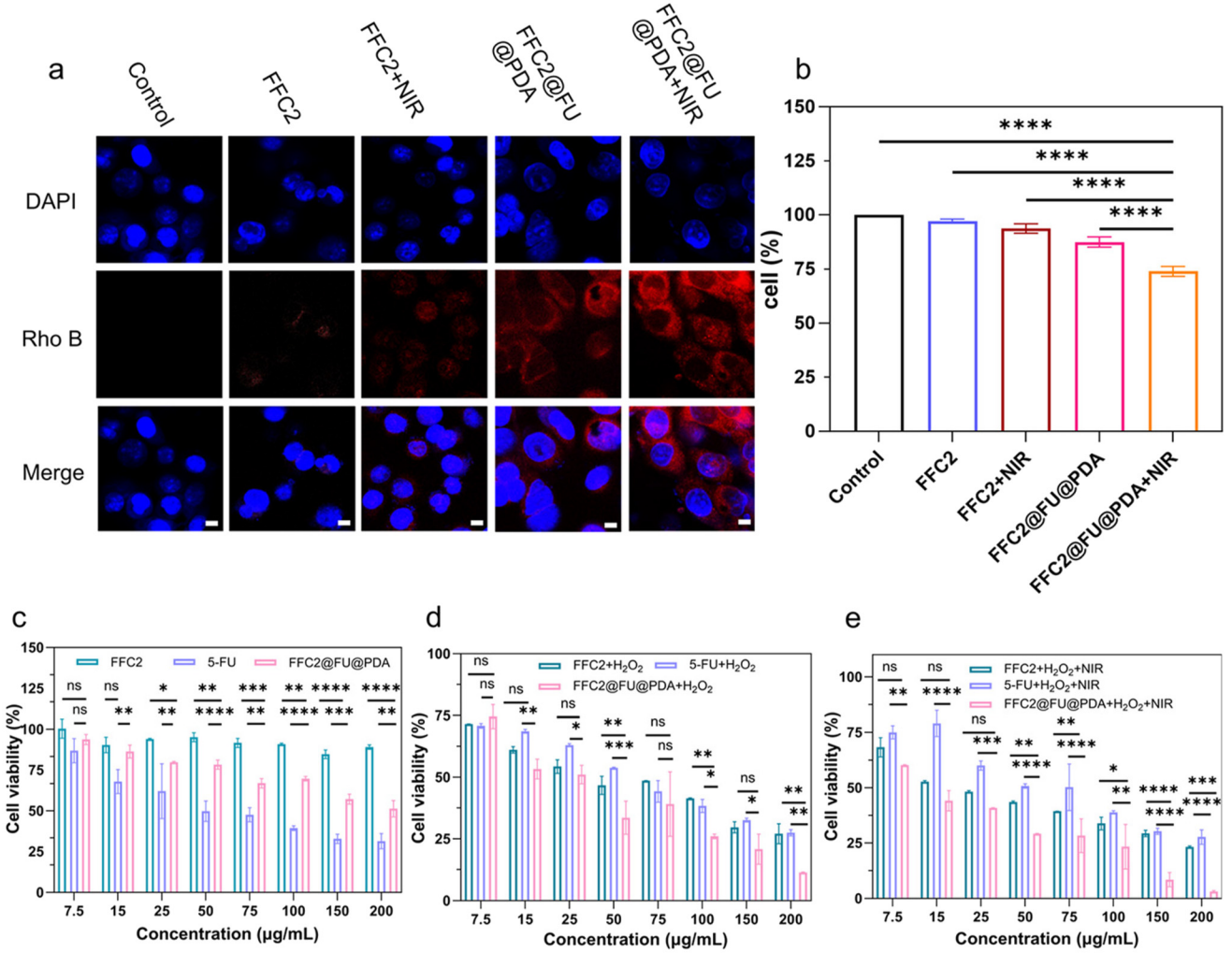

Fig. 4 (a) Uptake of materials by 4T1 cells (scale bar: 10 μm). (b) Semi-quantitative fluorescence analysis in 4T1 cells. (c–e) Viability of 4T1 cells after various treatments. Notes: *$P < 0.05$, **$P < 0.01$, ***$P < 0.001$, ****$P < 0.0001$.

ing progressively as drug concentration increased, reflecting its typical chemotherapeutic lethality. Interestingly, the drug-loaded group (FFC2@FU@PDA) shows weaker cytotoxic effects than the free drug group due to incomplete 5-FU release resulting from the sustained-release properties, further validating the controlled release advantage of the nanocarrier.

To validate the synergistic cell-killing efficacy of FFC2@FU@PDA under simulated TME conditions and NIR irradiation, CCK-8 assays, Calcein-AM/PI staining and scratch wound healing assays were systematically performed on 4T1 cells. As depicted in Fig. 4d, no significant difference in cell viability was observed between the free drug group (5-FU) and the TME-simulated group (H_2O_2 + 5-FU) (45–50%), suggesting that H_2O_2 does not alter drug sensitivity. For the CDT group (FFC2 + H_2O_2), cell viability significantly decreases to 37.5% at the highest concentration, primarily attributed to $^{\cdot}OH$ generation *via* Fe^{2+}-mediated Fenton reactions, which induced apoptosis. Strikingly, when FFC2@FU@PDA was combined with H_2O_2, cell viability dropped to 11.6% under the same conditions, demonstrating the synergistic interplay between ferroptosis mechanisms (driven by ROS generation) and 5-FU chemotherapy. This dual-action mechanism highlights the enhanced therapeutic efficacy achieved through simultaneous chemotherapeutic drug release and catalytic ROS production.

With the further introduction of NIR laser irradiation, the FFC2@FU@PDA + H_2O_2 + NIR combination group exhibits drastically amplified synergistic effects, reducing cell viability to approximately 3% at the highest concentration (Fig. 4e). This was attributed to the combined action of 5-FU and photothermal effects, which not only induced apoptosis but also exacerbated the intracellular acidic microenvironment, thereby significantly improving the efficiency of the Fenton reaction between Fe^{2+} and Fe^{3+} and dramatically enhancing the generation of $^{\cdot}OH$. This "chemotherapy-PTT-CDT" strategy enables spatiotemporally controlled ROS bursts and drug release, achieving multidimensional tumor cell eradication.[45]

Furthermore, scratch assays (Fig. S10) demonstrates that FFC2@FU@PDA suppressed 4T1 cell migration in a concentration-dependent manner compared to the control group. At equivalent treatment durations, higher nanoparticle concen-

trations correlated with stronger inhibitory effects on cell migration, underscoring its potential to curb tumor metastasis.

Based on the cell viability data obtained from the CCK-8 assay, Calcein-AM/PI staining was further employed to analyze cell death modes from morphological and membrane integrity perspectives. As shown in Fig. S11, the cells treated with 5-FU alone group (5-FU), chemotherapy alone group (H_2O_2 + 5-FU), drug-loaded material group (FFC2@FU@PDA), CDT alone group (H_2O_2 + FFC2), and chemotherapy + NIR group (H_2O_2 + 5-FU + NIR) exhibit enhanced red fluorescence (PI-positive signals) while retaining significant green fluorescence (Calcein-AM-positive signals), indicating that either CDT alone or single chemotherapy intervention failed to induce complete apoptosis. Notably, the introduction of 808 nm NIR irradiation does not significantly alter the red fluorescence intensity in these treatment groups, confirming the low absorption efficiency of 5-FU at this NIR wavelength and its inability to enhance cytotoxicity *via* photothermal effects.

Further analysis (Fig. 5a) reveals that both the H_2O_2 control group and the material-only group (FFC2) displayed wide-

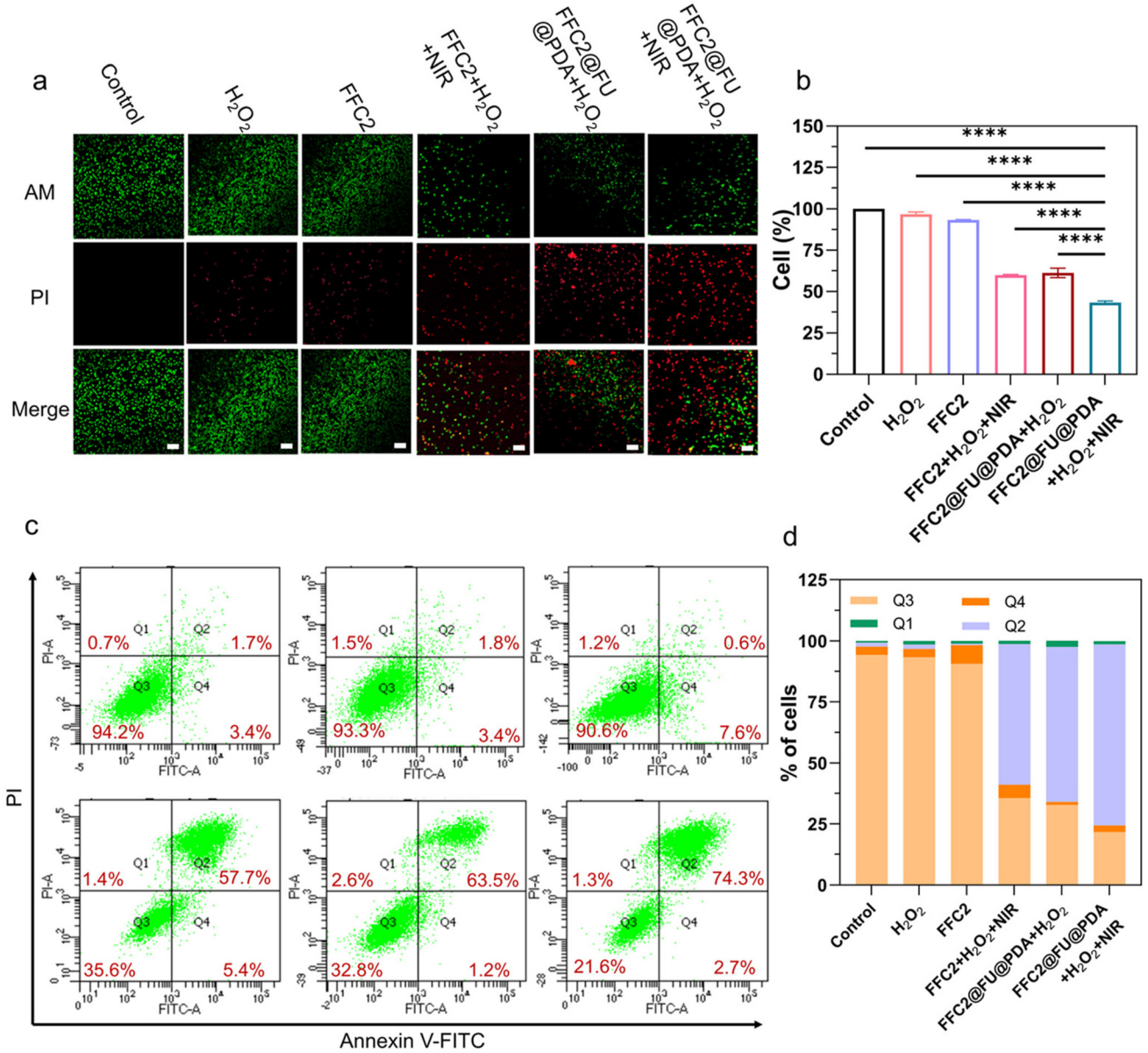

Fig. 5 (a) Representative confocal laser scanning microscopy images of 4T1 cells stained with Calcein-AM/PI under different experimental conditions (scale bar = 25 μm). (b) Semi-quantitative analysis of Calcein-AM/PI fluorescence intensity in 4T1 cells after various treatments. (c) Flow cytometry analysis of 4T1 cells stained with Annexin V-FITC/PI under different treatment conditions. The quadrants Q1, Q2, Q3, and Q4 represent necrotic, late apoptotic, viable, and early apoptotic cells, respectively. The numbers in each quadrant indicate the percentage of cells in the corresponding population. (d) Statistical histogram showing the percentage of cells in Q1, Q2, Q3, and Q4 quadrants after different treatments. Data are expressed as mean ± SD (n = 3). Notes: ****P < 0.0001.

spread green fluorescence in 4T1 cells, demonstrating that neither oxidative stress induced by H_2O_2 nor the material itself caused significant membrane damage. In contrast, the CDT + NIR combination group (H_2O_2 + FFC2 + NIR) shows markedly expanded red fluorescence regions, suggesting that the synergistic effect of CDT and PTT enhances cytotoxicity through membrane disruption. Strikingly, the final treatment group (triple-combination therapy: H_2O_2 + FFC2@FU@PDA + NIR) exhibits nearly complete loss of green fluorescence, with the majority of cells displaying red fluorescence, indicating that the combined action of 5-FU chemotherapy, CDT, and PTT profoundly disrupted membrane integrity, leading to massive cell death ($P < 0.0001$). Quantitative analysis (Fig. 5b) further demonstrates that the red fluorescence intensity in the CDT + NIR group, CDT + drug-loaded material group (H_2O_2 + FFC2@FU@PDA), and final treatment group increased by 3.4-fold, 4.1-fold, and 5.7-fold, respectively, compared to the control group, unequivocally validating that multi-mechanistic combination therapy significantly enhanced tumor cell killing *via* spatiotemporal synergy.

Furthermore, the Annexin V-FITC/PI apoptosis assay (Fig. S12) reveals that the viable cell proportions in the 5-FU alone, chemotherapy alone (H_2O_2 + 5-FU), drug-loaded material (FFC2@FU@PDA), CDT alone (H_2O_2 + FFC2), and chemotherapy + NIR (H_2O_2 + 5-FU + NIR) groups remain above 70%, confirming the limited efficacy of monotherapy in inducing apoptosis/necrosis. As shown in Fig. 5c and d, the H_2O_2 control and material-only groups (FFC2) maintain viable cell proportions exceeding 90%, with no significant difference from the blank control (control group), indicating negligible cytotoxicity from the material or baseline oxidative stress conditions. The CDT + NIR combination group (H_2O_2 + FFC2 +

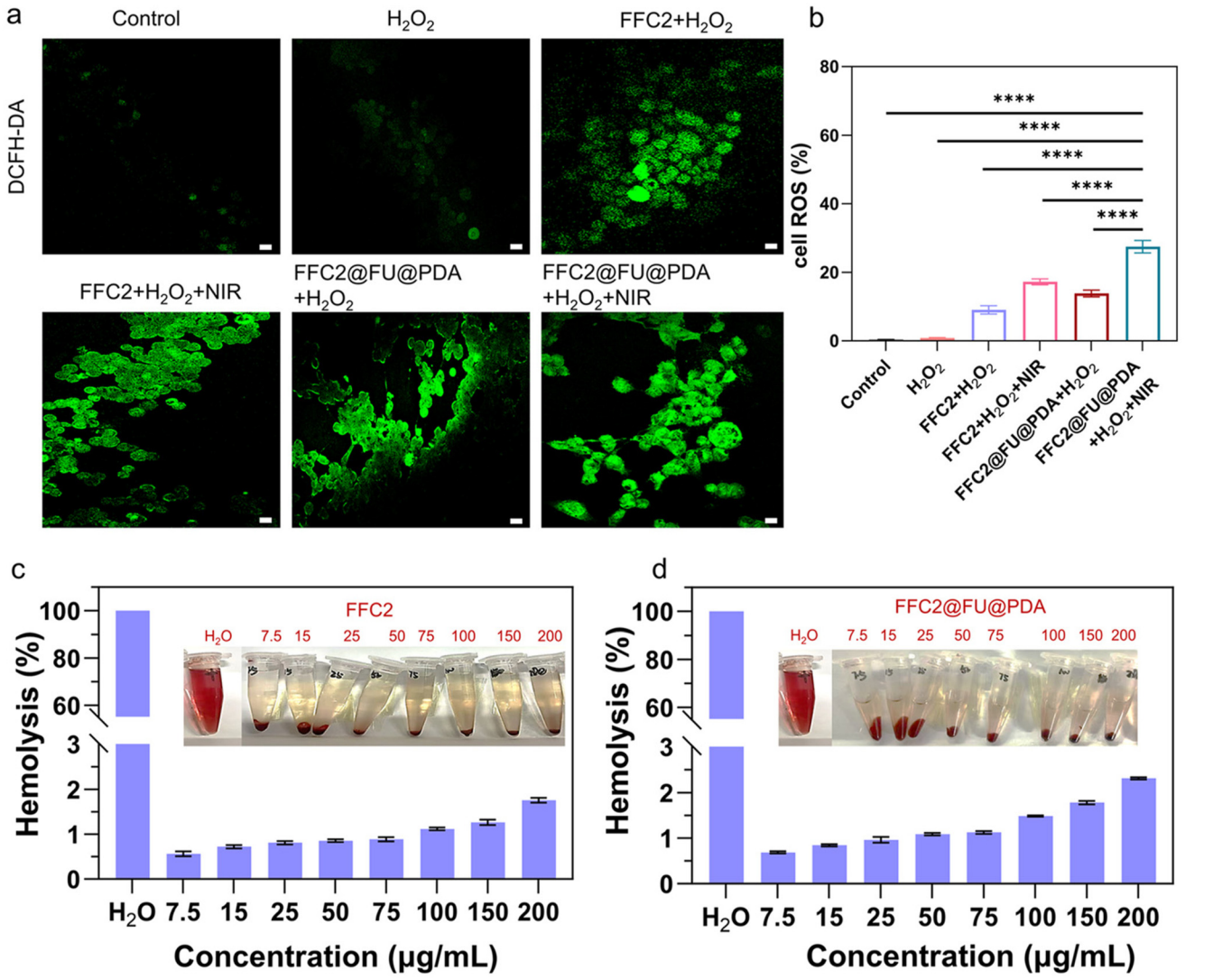

Fig. 6 (a) Confocal laser scanning microscopy images of DCFH-DA staining under different experimental conditions (scale bar = 20 μm). (b) Semi-quantitative analysis of DCFH-DA fluorescence intensity in 4T1 cells after treatment with different experimental conditions. (c) Hemolysis assay results of FFC2 at different concentrations. (d) Hemolysis assay results of FFC2@FU@PDA at different concentrations. Notes: ****$P < 0.0001$.

NIR) reduced the viable cell proportion to 35.6% through CDT-PTT synergy, representing a breakthrough improvement compared to the CDT-alone group (H_2O_2 + FFC2 group: 63.2%). The triple-combination therapy group (H_2O_2 + FFC2@FU@PDA + NIR) further decreases the viable cell proportion to 21.6%, achieving a 14% reduction relative to the CDT + NIR group, highlighting the superior efficacy of the triple-combination strategy in promoting apoptosis/necrosis. These results align with the Calcein-AM/PI staining data, systematically demonstrating that the combined therapeutic strategy synergistically enhances antitumor efficacy through multi-dimensional mechanisms, including metabolic suppression (CCK-8), membrane integrity disruption (Calcein-AM/PI), and apoptosis/necrosis induction (annexin V/PI).

3.5. ROS generation capacity and hemolytic activity assessment

Previous studies confirmed that FFC2 catalyzes the generation of $^{\bullet}OH$ from H_2O_2 *via* the Fenton reaction extracellularly. Given the acidic nature and H_2O_2 overexpression in the TME,[46] intracellular reactive oxygen species (ROS) levels in 4T1 cells under various treatment conditions were further investigated using

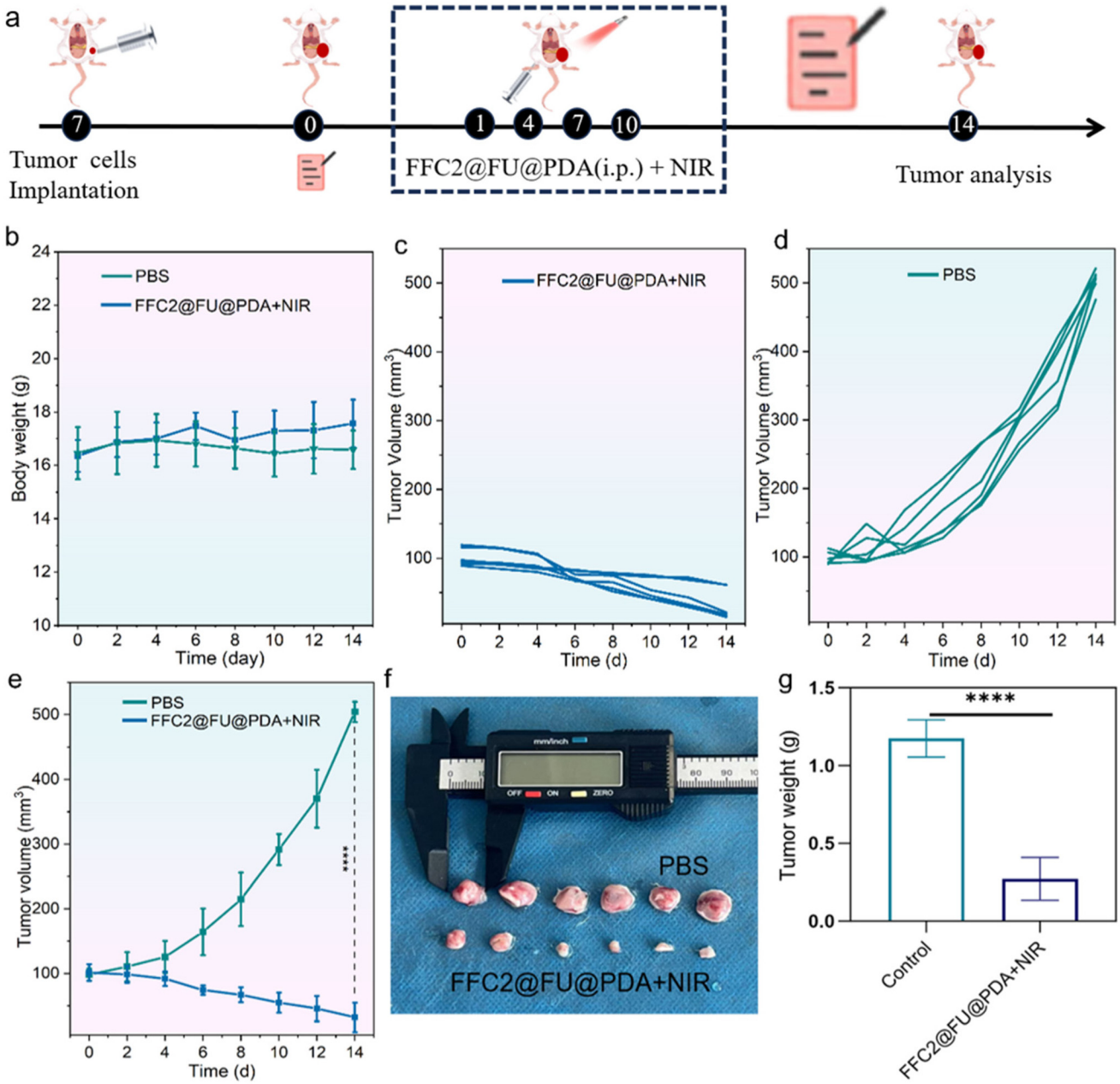

Fig. 7 (a) The evaluation of the antitumor ability of FFC2@FU@PDA + NIR in mice. (b) The monitoring of the body weight of mice in different treatment groups during the treatment period. Tumor growth curve of tumor-bearing mice after treatment with FFC2@FU@PDA + NIR (c) and PBS (d). (e) Changes in tumor volume of different groups. (f) Photograph of the excised tumor on day 14. (g) Tumor weight after dissection day 14.

the DCFH-DA fluorescent probe, a membrane-permeable compound that undergoes ROS-dependent oxidation to produce green fluorescent dichlorofluorescein (DCF). As shown in Fig. S13, no significant green fluorescence signals were detected in the material-only group (FFC2), drug-only group (5-FU), drug treatment group (H_2O_2 + 5-FU), drug-loaded material group (FFC2@FU@PDA), or drug treatment + NIR group (H_2O_2 + 5-FU + NIR), indicating negligible ROS generation under these conditions.

Further analysis (Fig. 6a and b) reveals that the fluorescence intensity of the H_2O_2 control group shows no statistical difference from the blank control group, confirming that H_2O_2 cannot spontaneously decompose to produce ROS in the absence of Fe^{2+}. In contrast, the CDT group (H_2O_2 + FFC2) under simulated TME conditions (with exogenous H_2O_2) exhibits a pronounced fluorescence signal, demonstrating effective activation of the Fenton reaction. The fluorescence intensity in the CDT + NIR group (H_2O_2 + FFC2 + NIR) increased by 5.7-fold compared to the control group, suggesting that NIR-induced photothermal effects enhance Fenton reaction kinetics, likely through localized heating to accelerate Fe^{2+}/Fe^{3+} cycling or reaction rates. Notably, the combined chemo-CDT-PTT group (H_2O_2 + FFC2@FU@PDA + NIR) achieves a fluorescence intensity 9.0-fold higher than the control group, significantly surpassing all other groups ($P < 0.0001$). This implies that 5-FU may synergize with PTT to amplify TME acidity *via* cellular stress induction, thereby optimizing Fenton reaction conditions and enabling cascaded ROS amplification.[40,47]

Hemolysis assay results (Fig. 6c and d) demonstrate that both FFC2 and FFC2@FU@PDA at concentrations of 7.5–200 μg mL^{-1} induced hemolysis rates below 2.5% (2.29% for the 200 μg mL^{-1} FFC2@FU@PDA group) after 2 h of incubation, compliant with the ISO 10993-4 biocompatibility standard for medical materials (hemolysis rate <5%). These data confirm that neither FFC2 nor FFC2@FU@PDA caused significant erythrocyte rupture within the tested concentration range, supporting their potential safety for injectable applications.

3.6. *In vivo* tumor assay

Following confirmation of the potent anti-tumor efficacy of FFC2@FU@PDA + NIR at the cellular level, we further evaluated its *in vivo* therapeutic performance in a 4T1 tumor-bearing mouse model (Fig. 7a). The FFC2@FU@PDA + NIR group received near-infrared (NIR) laser irradiation (2 W cm^{-2}, 5 min) 24 h post intraperitoneal injection. As shown in Fig. 7b, no significant differences in body weight changes were observed among the groups during the treatment period, indicating minimal systemic metabolic impact and favorable safety profile of the therapeutic system. Tumor volume monitoring results (Fig. 7c–e) reveal a significant reduction in tumor volume in the FFC2@FU@PDA + NIR treatment group compared to the PBS control group. This effect is primarily attributed to the synergistic advantage of the triple-modality therapy combining chemotherapy, photothermal therapy, and chemodynamic therapy. The efficacy of FFC2@FU@PDA + NIR was further corroborated by assessing the weight and gross morphology of the excised tumors: tumors in the treatment group exhibited significant shrinkage (Fig. 7f and g), consistent with the volume reduction trend, whereas control group tumors were larger. Statistical analysis demonstrated a significantly higher tumor growth inhibition rate in the FFC2@FU@PDA + NIR group compared to the blank control group (reaching 17-fold that of the control group). Importantly, no mouse mortality events were observed throughout the experiment, further validating the excellent biocompatibility and low toxicity of this drug delivery system.

4. Conclusions

In this study, a multifunctional Fe_3O_4–Fe_3C heterostructure anchored on carbon nanosheets was synthesized through tannic acid-Fe^{3+} coordination, controlled pyrolysis, and selective HCl etching. The material synergistically integrates enhanced magnetization for magnetic targeting, a high specific surface area carbon matrix high drug-loading capacity, and high content of Fe^{2+} species for enhancing Fenton reaction kinetics. Subsequent 5-FU loading and PDA coating endowed the system with pH-responsive drug release (55.6% loading efficiency) and exceptional photothermal performance. Both *in vitro* and *in vivo* studies confirm the pronounced tumor-inhibitory efficacy of tumor microenvironment-activated triple-modality therapy. This work overcomes the limitations of traditional Fe_3O_4 nanomaterials by enhancing both magnetic and photothermal performance, offering an innovative strategy for multimodal cancer therapy with robust clinical translation potential.

Author contributions

Desheng Wang: conceptualization, methodology, formal analysis, investigation, data curation, writing – original draft. Changjin Xu: methodology, formal analysis, investigation, writing – review & editing, funding acquisition. Shikui Wu: formal analysis, funding acquisition. Gang Li: resources. Huiwen Zhang: conceptualization, methodology. Herima Qi: methodology. Riqing Cheng: methodology. Liang Bao: methodology. Huiqing Guo: methodology, formal analysis, funding acquisition, resources, supervision. Jianping Chen: methodology, formal analysis, funding acquisition, resources, supervision.

Conflicts of interest

The authors declare that they have no conflict of interest.

Data availability

The data that support the findings of this study are available from the corresponding author upon reasonable request.

Supplementary information (SI) is available. See DOI: https://doi.org/10.1039/d5dt02555a.

Acknowledgements

The work was supported by the National Natural Science Foundation of China (22168029 and 82360824), the Natural Science Foundation of Inner Mongolia (2024QN05006), the Foundation of Inner Mongolia Medical University (YKD2023MS082 and YKD2025ZD009), the Doctoral Start-up Fund Project of Inner Mongolia Medical University (YKD2025BSQD022 and YKD2024BSQD009) and the Program for Yong Talents of Science and Technology in Universities of Inner Mongolia Autonomous Region.

References

1 S. Wang, Y. Zhang, Y. Li, K. Chen, Y. Dai, D. Zhou, A. Ali, S. Yang, X. Xu, T. Jiang and L. Zhu, Au nanostars@PDA@Fe_3O_4-based multifunctional nanoprobe for integrated tumor diagnosis and photothermal therapy, *Mater. Des.*, 2021, **205**, 109707.

2 Y. Chen, M. Su, L. Jia and Z. Zhang, Synergistic Chemo-photothermal and ferroptosis therapy of polydopamine nanoparticles for esophageal cancer, *Nanomedicine*, 2022, **17**, 1115–1130.

3 M. Li, X. Wan, B. Shan, Y. He, C. Chen and M. Shen, A pH and GSH dual responsive nanoparticle co-deliver adriamycin and olaparib enhanced the therapeutic efficacy on triple negative breast cancer, *Mater. Des.*, 2025, **256**, 114271.

4 J. Ben-Dror, M. Shalamov and A. Sonnenblick, The history of early breast cancer treatment, *Genes*, 2022, **13**, 960.

5 Y. Hao, T. Liu, R. Xu, B. Li, K. Li and Y. Chen, Tumor penetrating Janus prodrug nanoassemblies for enhanced synergistic chemotherapy and photodynamic therapy of colon cancer, *Mater. Des.*, 2024, **241**, 112974.

6 M. Wang, W. Liu, Y. Zhang, M. Dang, Y. Zhang, J. Tao, K. Chen, X. Peng and Z. Teng, Intercellular adhesion molecule 1 antibody-mediated mesoporous drug delivery system for targeted treatment of triple-negative breast cancer, *J. Colloid Interface Sci.*, 2019, **538**, 630–637.

7 R. Cui, P. Zhao, Y. Yan, G. Bao, A. Damirin and Z. Liu, Outstanding Drug-loading/release capacity of hollow Fe-metal–organic framework-based microcapsules: a potential multifunctional drug-delivery platform, *Inorg. Chem.*, 2021, **60**, 1664–1671.

8 J. Li, D. Yang, W. Lyu, Y. Yuan, X. Han, W. Yue, J. Jiang, Y. Xiao, Z. Fang, X. Lu, W. Wang and W. Huang, A bioinspired photosensitizer performs tumor thermoresistance reversion to optimize the atraumatic mild–hyperthermia photothermal therapy for breast cancer, *Adv. Mater.*, 2024, **36**, 2405890.

9 M.-Y. Xu, J. Zeng, X.-H. Han, D.-D. Wei, B. Fan, X. Qu, S. Huang and X.-J. Han, Single component organic photosensitizer for tumor photodynamic/photothermal immunotherapy via apoptosis and pyroptosis, *Mater. Des.*, 2025, **251**, 113647.

10 W. Ying, Y. Zhang, W. Gao, X. Cai, G. Wang, X. Wu, L. Chen, Z. Meng, Y. Zheng, B. Hu and X. Lin, Hollow magnetic nanocatalysts drive starvation–chemodynamic–hyperthermia synergistic therapy for tumor, *ACS Nano*, 2020, **14**, 9662–9674.

11 Q. Yang, L. Xu, J. Wang, X. Cai, S.-Y. Lu, Q. Zhang, Y. Duan, M. Wang and H. Liu, Iron-decorated, IR820-loaded polypyrrole nanocomposites for synergistic tumor photothermal, photodynamic, and chemodynamic therapy, *J. Nanopart. Res.*, 2022, **24**, 8.

12 M. Lyu, D. Zhu, X. Kong, Y. Yang, S. Ding, Y. Zhou, H. Quan, Y. Duo and Z. Bao, Glutathione–depleting nanoenzyme and glucose oxidase combination for hypoxia modulation and radiotherapy enhancement, *Adv. Healthcare Mater.*, 2020, **9**, 1901819.

13 C. Wen, X. Guo, C. Gao, Z. Zhu, N. Meng, X.-C. Shen and H. Liang, NIR-II-responsive AuNRs@SiO_2–RB@MnO_2 nanotheranostic for multimodal imaging-guided CDT/PTT synergistic cancer therapy, *J. Mater. Chem. B*, 2022, **10**, 4274–4284.

14 J. Wang, Y. Zhang, M. Dong, Z. Liu, B. Guo, H. Zhang and L. Gao, Capture and release of circulating tumor cells stimulated by pH and NIR irradiation of magnetic Fe_3O_4@ZIF-8 nanoparticles, *Colloids Surf., B*, 2023, **224**, 113206.

15 H. Sun, X. Wang, Z. Guo, Z. Hu, Y. Yin, S. Duan, W. Jia, W. Lu and J. Hu, Fe_3O_4 nanoparticles that modulate the polarisation of tumor-associated macrophages synergize with photothermal therapy and immunotherapy (PD-1/PD-L1 inhibitors) to enhance anti-tumor therapy, *Int. J. Nanomed.*, 2024, **19**, 7185–7200.

16 S. Jafari, M. Soleimani and R. Salehi, Nanotechnology-based combinational drug delivery systems for breast cancer treatment, *Int. J. Polym. Mater. Polym. Biomater.*, 2019, **68**, 859–869.

17 M. J. Mitchell, M. M. Billingsley, R. M. Haley, M. E. Wechsler, N. A. Peppas and R. Langer, engineering precision nanoparticles for drug delivery, *Nat. Rev. Drug Discovery*, 2021, **20**, 101–124.

18 Y. P. Yew, K. Shameli, M. Miyake, N. B. B. A. Khairudin, S. E. B. Mohamad, T. Naiki and K. X. Lee, Green biosynthesis of superparamagnetic magnetite Fe_3O_4 nanoparticles and biomedical applications in targeted anticancer drug delivery system: A review, *Arabian J. Chem.*, 2020, **13**, 2287–2308.

19 G. Lv, G. Wang, Q. Wang, W. Li, P. Zhao, X. Meng, L. Sun, Y. Wu, L. Guo, Y. Yan and X. Jiang, Dual-radical generating FePEIDN nanocomposite for tumor therapy: sulfite radical persistence meets fenton catalysis, *Mater. Des.*, 2025, **253**, 113960.

20 J. Yu, F. Chen, W. Gao, Y. Ju, X. Chu, S. Che, F. Sheng and Y. Hou, Iron carbide nanoparticles: an innovative nanoplatform for biomedical applications, *Nanoscale Horiz.*, 2017, **2**, 81–88.

21 Y. Ju, H. Zhang, J. Yu, S. Tong, N. Tian, Z. Wang, X. Wang, X. Su, X. Chu, J. Lin, Y. Ding, G. Li, F. Sheng and Y. Hou,

Monodisperse Au–Fe_2C Janus nanoparticles: an attractive multifunctional material for triple-modal imaging-guided tumor photothermal therapy, *ACS Nano*, 2017, **11**, 9239–9248.

22 J. Yu, F. Zhao, W. Gao, X. Yang, Y. Ju, L. Zhao, W. Guo, J. Xie, X. Liang, X. Tao, J. Li, Y. Ying, W. Li, J. Zheng, L. Qiao, S. Xiong, X. Mou, S. Che and Y. Hou, Magnetic reactive oxygen species nanoreactor for switchable magnetic resonance imaging guided cancer therapy based on pH-sensitive Fe_5C_2 @Fe_3O_4 nanoparticles, *ACS Nano*, 2019, **13**, 10002–10014.

23 Z. Yang, T. Zhao, X. Huang, X. Chu, T. Tang, Y. Ju, Q. Wang, Y. Hou and S. Gao, Modulating the phases of iron carbide nanoparticles: from a perspective of interfering with the carbon penetration of Fe@Fe_3O_4 by selectively adsorbed halide ions, *Chem. Sci.*, 2017, **8**, 473–481.

24 J. Yu, Y. Ju, L. Zhao, X. Chu, W. Yang, Y. Tian, F. Sheng, J. Lin, F. Liu, Y. Dong and Y. Hou, Multistimuli-regulated photochemothermal cancer therapy remotely controlled via Fe_5C_2 Nanoparticles, *ACS Nano*, 2016, **10**, 159–169.

25 Y. Zhang, R. Ning, W. Wang, Y. Zhou and Y. Chen, Synthesis of Fe_3O_4/PDA nanocomposites for osteosarcoma magnetic resonance imaging and photothermal therapy, *Front. Bioeng. Biotechnol.*, 2022, **10**, 844540.

26 A. S. Hadi, M. Haghi, A. Barzegar, M. Ali and H. Feizi, Comparative evaluation of hesperetin-loaded graphene oxide nanosheets (Hsp-GO) as a drug delivery system for colon cancer: synthesis and anticancer efficiency assessment, *Mol. Biol. Rep.*, 2024, **51**, 591.

27 T. Ma, S. Xu and M. Zhu, Hierarchical porous carbon based on waste quinoa straw for high-performance supercapacitors, *ACS Omega*, 2024, **9**, 13592–13602.

28 W. Cai, M. Guo, X. Weng, W. Zhang, G. Owens and Z. Chen, Modified green synthesis of Fe_3O_4@SiO_2 nanoparticles for pH responsive drug release, *Mater. Sci. Eng., C*, 2020, **112**, 110900.

29 D. He, M. Sun, D. Cao, Y. Ding, H. Chen and G. He, Flexible free-standing Fe_2O_3 nanoparticle/carbon shells/graphene films for advanced lithium-ion batteries, *ACS Appl. Nano Mater.*, 2022, **5**, 5017–5024.

30 Y. Pan, C. Luo, D. Yang, P. Sun, J. Chen, Z. Sui and Q. Tian, Ultrathin porous Fe_2O_3@C nanosheets: novel preparation strategy and high lithium storage, *Appl. Surf. Sci.*, 2023, **635**, 157763.

31 Y. Zheng, H. Xiao, K. Li, Y. Wang, Y. Li, Y. Wei, X. Zhu, H.-W. Li, D. Matsumura, B. Guo, F. He, X. Chen and H. Wang, Ultra-fine CeO_2 particles triggered strong interaction with $LaFeO_3$ framework for total and preferential CO oxidation, *ACS Appl. Mater. Interfaces*, 2020, **12**, 42274–42284.

32 J. Su, D. Pan, Y. Dong, Y. Zhang, Y. Tang, J. Sun, L. Zhang, Z. Tian and L. Chen, Ultrafine Fe_2C iron carbide nanoclusters trapped in topological carbon defects for efficient electroreduction of carbon dioxide, *Adv. Energy Mater.*, 2023, **13**, 2204391.

33 G. Qian, L. Zhang, X. Li, C. Shuai and X. Wang, Construction of Fe_3O_4 -loaded mesoporous carbon systems for controlled drug delivery, *ACS Appl. Bio Mater.*, 2021, **4**, 5304–5311.

34 M. Wang, Z. Shu, L. Zhang, X. Fan, G. Tao, Y. Wang, L. Chen, M. Wu and J. Shi, Amorphous Fe^{2+}-rich FeO_x loaded in mesoporous silica as a highly efficient heterogeneous fenton catalyst, *Dalton Trans.*, 2014, **43**, 9234–9241.

35 J. Lu, Q. Zou, Y. Li, C. Xiong, L. Tao, J. Wu, M. Qin, J. Yang, L. He, M. Qin, M. Dong, Y. Li and S. Cao, FTH1P8 induces and transmits docetaxel resistance by inhibiting ferroptosis in prostate cancer, *Biomed. Pharmacother.*, 2024, **180**, 117472.

36 J. Yang, B. Ren, H. Cai, W. Xiong, J. Feng, Q. Fan, Z. Li, L. Huang, C. Yan, Y. Li, C. Chen and Z. Shen, Cyclic catalysis of intratumor $Fe^{3+/2+}$ initiated by a hollow mesoporous iron sesquioxide nanoparticle for ferroptosis therapy of large tumors, *Biomaterials*, 2025, **313**, 122793.

37 H. Zheng, L. Huang, G. An, L. Guo, N. Wang, W. Yang and Y. Zhu, A nanoreactor based on metal–organic frameworks with triple synergistic therapy for hepatocellular carcinoma, *Adv. Healthcare Mater.*, 2024, **13**, 2401743.

38 K. Zhang, Y. Bai, R. Xu, J. Li and F. Guan, The mechanism of PDA/PEI/5–Fu coated esophageal stent material on inhibiting cancer associated pathological cells, *J. Biomed. Mater. Res., Part A*, 2020, **108**, 814–821.

39 S. Cheralayikkal, K. Manoj and K. P. S. Hussan, Formulation and evaluation of a smart drug delivery system of 5-fluorouracil for pH-sensitive chemotherapy, *Heliyon*, 2022, **8**, e09926.

40 H. Dai, A. Han, X. Wang, P. Zhu, D. Wang and Y. Wang, NIR-triggering cobalt single-atom enzyme switches off-to-on for boosting the interactive dynamic effects of multimodal phototherapy, *Nat. Commun.*, 2025, **16**, 2058.

41 W. Zhang, W. Lin, X. Wang, C. Li, S. Liu and Z. Xie, Hybrid nanomaterials of conjugated polymers and albumin for precise photothermal therapy, *ACS Appl. Mater. Interfaces*, 2019, **11**, 278–287.

42 H.-J. Yoon, H.-S. Lee, J.-Y. Lim and J.-H. Park, Liposomal indocyanine green for enhanced photothermal therapy, *ACS Appl. Mater. Interfaces*, 2017, **9**, 5683–5691.

43 H. Deng, J. Zhang, Y. Yang, J. Yang, Y. Wei, S. Ma and Q. Shen, Chemodynamic and photothermal combination therapy based on dual-modified metal–organic framework for inducing tumor ferroptosis/pyroptosis, *ACS Appl. Mater. Interfaces*, 2022, **14**, 24089–24101.

44 D. Ren, G. R. Williams, Y. Zhang, R. Ren, J. Lou and L.-M. Zhu, Mesoporous doxorubicin-loaded polydopamine nanoparticles coated with a platelet membrane suppress tumor growth in a murine model of human breast cancer, *ACS Appl. Bio Mater.*, 2022, **5**, 123–133.

45 J. Li, Z. Chen, Z. Pei and Y. Pei, A hyaluronic acid modified advanced nanoagent activated by tumor microenvironment enables a reciprocal dual-modality therapy, *Chem. Eng. J.*, 2025, **507**, 159884.

46 J. Li, Y. Li, Y. Wang, W. Jin, Z. Pei, Y. Lv and Y. Pei, A proton pump inhibitor-programmed ROS generator enhances the synergistic efficacy of chemo-/chemodynamic therapy with reduced renal injury, *Chem. Eng. J.*, 2025, **505**, 159201.

47 W. Jin, Z. Chen, Y. Wang, J. Li, J. Li, Y. Pei and Z. Pei, Nano metal-photosensitizer based on Aza-BODIPY-Cu complex for CDT-enhanced dual phototherapy, *Chin. Chem. Lett.*, 2024, **35**, 109328.